Flexible PV-cell Modeling for Energy Harvesting in Wearable IoT Applications

JAEHYUN PARK and HITESH JOSHI, Arizona State University HYUNG GYU LEE, Daegu University SAYFE KIAEI and UMIT Y. OGRAS, Arizona State University

Wearable devices with sensing, processing and communication capabilities have become feasible with the advances in internet-of-things (IoT) and low power design technologies. Energy harvesting is extremely important for wearable IoT devices due to size and weight limitations of batteries. One of the most widely used energy harvesting sources is photovoltaic cell (PV-cell) owing to its simplicity and high output power. In particular, flexible PV-cells offer great potential for wearable applications. This paper models, for the first time, how bending a PV-cell significantly impacts the harvested energy. Furthermore, we derive an analytical model to quantify the harvested energy as a function of the radius of curvature. We validate the proposed model empirically using a commercial PV-cell under a wide range of bending scenarios, light intensities and elevation angles. Finally, we show that the proposed model can accelerate maximum power point tracking algorithms and increase the harvested energy by up to 25.0%.

CCS Concepts: • Hardware → Renewable energy; Platform power issues; Modeling and parameter extraction;

Additional Key Words and Phrases: Flexible hybrid electronics (FHE), wearable IoT devices, PV-cell model, power estimation, MPPT

ACM Reference format:

Jaehyun Park, Hitesh Joshi, Hyung Gyu Lee, Sayfe Kiaei, and Umit Y. Ogras. 2017. Flexible PV-cell Modeling for Energy Harvesting in Wearable IoT Applications. *ACM Trans. Embed. Comput. Syst.* 16, 5s, Article 156 (September 2017), 20 pages.

https://doi.org/10.1145/3126568

1 INTRODUCTION

Wearable devices interweave technology into daily life in a myriad of applications including health monitoring, smart watch, and fitness tracker. Widespread adoption of these devices is hindered by the duration they can operate without recharging. Since the weight, size and flexibility constraints limit the total battery capacity [7], it is imperative to leverage ambient energy sources, such as solar

This article was presented in the International Conference on Hardware/Software Codesign and System Synthesis (CODES+ISSS) 2017 and appears as part of the ESWEEK-TECS special issue.

This work was supported by NSF CAREER award CNS-1651624 and in part by the Basic Science Research Program through the National Research Foundation of Korea (NRF), funded by the Ministry of Education (NRF-2017R1D1A1B03032382). Author's addresses: J. Park, H. Joshi, S. Kiaei, and U. Y. Ogras, School of Electrical, Computer and Energy Engineering, Arizona State University, Tempe, AZ 85287; emails: {jpark244, hjoshi5, sayfe, umit}@asu.edu; H. G. Lee, School of Computer and Communication Engineering, Daegu University, South Korea 38453; email: hglee@daegu.ac.kr.

Permission to make digital or hard copies of all or part of this work for personal or classroom use is granted without fee provided that copies are not made or distributed for profit or commercial advantage and that copies bear this notice and the full citation on the first page. Copyrights for components of this work owned by others than ACM must be honored. Abstracting with credit is permitted. To copy otherwise, or republish, to post on servers or to redistribute to lists, requires prior specific permission and/or a fee. Request permissions from permissions@acm.org.

© 2017 ACM 1539-9087/2017/09-ART156 \$15.00

https://doi.org/10.1145/3126568

156:2 J. Park et al.

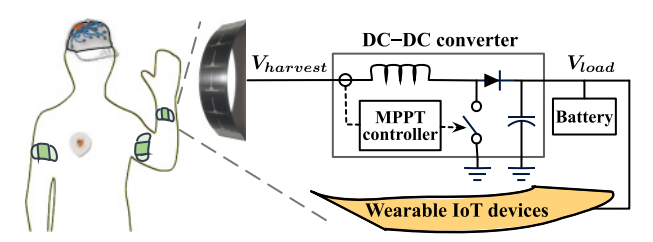


Fig. 1. Wearable IoT devices powered by a flexible PV-cell.

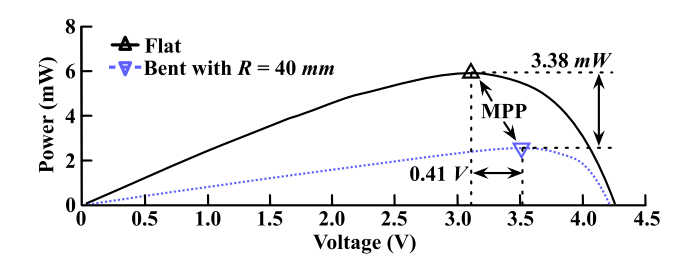


Fig. 2. The P-V curve of a flexible PV-cell for a constant radiation intensity $G = 1000 \ W/m^2$ and elevation angle $\alpha = 50^{\circ}$ when is flat and bent.

energy, body heat and motion. We envision an application scenario where the wearable device is primarily powered through the harvested energy with a small battery serving as a backup, as shown in Figure 1. Flexible harvesting sources are necessary for wearable applications, since they can conform to human body and clothing. Flexible photovoltaic cells (PV-cells), in particular, offer superior outdoor and competitive indoor power density to other alternatives. They can deliver $10-100~mW/cm^2$ outdoors and $100~\mu W/cm^2$ indoors [19]. In comparison, flexible thermoelectric generators (TEG) generate 3.8 mW/cm^2 at $\Delta T=50~K$ [10] and piezoelectric generators provide up to $101~\mu W/cm^3$ with 1~kgf [9].

The amount of power harvested from a PV-cell is determined by the operating point on the current–voltage (I–V) curve. The voltage and current values that maximize the harvested power is called the maximum power point (MPP). Both the MPP and harvested power are a strong function of the physical flexibility of a PV-cell. To demonstrate this impact, we performed experiments with a rectangular FlexSolarCell flexible PV SP3-12 unit with length L=50.8~mm and width W=12.7~mm [6]. We observe that the power produced by this unit degrades significantly under bending. In particular, R=40~mm radius of curvature leads to 56.7% degradation in maximum harvested power, for a constant radiation intensity G. Our measurements also show that the MPP can change significantly when the PV-cell is bent, as illustrated using the \triangle and ∇ markers in Figure 2. Therefore, finding the location of the MPP is important to maximize the harvested power. Furthermore, PV models, such as Sandia PV Array Performance Model [11] and parameter extraction methods [21], rely on it to reproduce the I-V curve.

The MPP changes as a function of the load current, radiation and temperature. Therefore, a variety of maximum power point tracking (MPPT) algorithms are proposed to maximize the harvested power [2, 5, 20]. MPPT algorithms run in conjunction with a DC–DC converter and an MPPT controller. The controller regulates input voltage or current of the converter, as shown in Figure 1. For example, the maximum power point voltage V_{MPP} decreases (increases) as the radiation intensity reduces (grows), while the ratio of the V_{MPP} to the open circuit voltage, i.e., (V_{MPP}/V_{OC}) , does not

vary significantly for flat PV-cells [2]. Fractional open-circuit voltage (FOCV) MPPT algorithm utilizes this information to track V_{MPP} .

Two major considerations of MPPT algorithms are accelerating the convergence time and minimizing the tracking energy overhead. When the MPP shifts due to a rapid change in operating conditions, the MPPT algorithms dynamically search for the new MPP. This search happens incrementally, unless there is a model that predicts the change in the MPP. The approach presented in [12, 24] shows that estimating the new MPP reduces the convergence time when a sudden radiation change occurs. In Section 4.3, we show that bending can also change the parameters of the MPPT algorithm significantly compared to a flat PV-cell model. Although the impact of bending on the harvested power is well established, *to date*, there are no analytical models that quantify this relation. An analytical quantification can accelerate the MPPT algorithms and boost the harvested power in flexible PV-cells. Moreover, it can be used to predict the energy harvesting potential given an application scenario, e.g., when wearing the flexible PV-cell on the arm.

In this paper, we first model the radiation received by the flexible PV-cell as a function of the radius of curvature, the radiation intensity, and the incident angle of light source to the PV-cell's surface. Then, we extend the proposed model to account for the partial shading effect that causes significant change in the harvested power. We validate the accuracy of the proposed model by comparing an exhaustive set of empirical results that includes using a commercial FlexSolarCell (PV SP3-12 unit). Our extensive validation demonstrates that the proposed model can predict the voltage and power at the maximum power point with 1.8% and 4.8% error, respectively. Finally, we use our analytical models to extract the circuit parameters of flexible PV-cells. The proposed models and extracted parameters enable us to accelerate the MPPT algorithms and boost the harvested power. Our simulations performed using a fractional open-circuit voltage MPPT algorithm [2] show that the proposed analytical model increases the harvested energy by as much as 25.0%.

The major contributions of this work are as follows:

- We derive an analytical model that quantifies the I-V characteristics of flexible PV-cells under different bending and partial shading scenarios
- Our exhaustive experiments using a commercial PV-cell show that we can estimate the voltage and power at the MPP on average with 1.8% and 4.8% error, respectively.
- We show that the proposed model leads up to 25.0% increase in harvested energy compared to a MPPT algorithm that does not model flexibility

The rest of this paper is organized as follows. Section 2 reviews the related work and highlights our major contributions. The analytical radiation model with bending is derived in Section 3. We present validation of the proposed model with extensive experiments and show the benefit of the model in Section 4. Finally, Section 5 concludes this paper.

2 RELATED WORK

Designing the power supply system is a key issue for IoT applications, since insufficient power can severely limit their operation. Accurate analytical modeling is proven to be a good starting point for low power system design [14]. Hence, analytical modeling of flexible PV-cells is an important problem, which has not been addressed before.

A two-fold three dimensional PV panel, instead of a traditional two-dimensional flat PV panel is proposed in [25]. Similar to our approach, this work analyzes the power change of the two-fold three-dimensional PV panel as a function of the angle between the sub-panels. It also discusses the partial shading effects, which is an important problem. This work extends the service time of applications, but it still targets only flat PV-cells. Thus, their models are not suitable for considering the flexible PV-cells. Power generated by PV-cells degrades significantly, if one of the serially

156:4 J. Park et al.

connected cells has lower radiation intensity than the others. The cell with lower radiation not only provides less power but also hinders power generation of other cells [31]. This phenomenon can be avoided with help of bypass diodes, which generates local maximum power points [13, 22, 23]. Therefore, we explicitly model the impact of partial shading and bypass diodes.

Uneven distribution of radiation intensity across a bent PV is an inherent feature of flexible PV-cells. A simple equation to calculate the effective length of a flexible PV-cell, when it is bent, is proposed in [13]. However, the authors do not present an analytical model, but only measure the behavior of flexible PV-cells to develop an MPPT algorithm. The ratio of the maximum harvested power P_{MPP} to the product of open-circuit voltage V_{OC} and short-circuit current I_{SC} , i.e., fill factor, can be used to model the behavior of PV-cells. The work presented in [22] models flexible PV-cells based on the fill factor, which changes with bending. Their method requires a set of measured data at different bending scenarios. Furthermore, it is not able to find the location of local maximum power point caused by bypass diodes. In contrast, our approach requires measurements only for flat cells and finds the local and global MPPs with or without bypass diodes.

In energy harvesting applications, maximum power point tracking has been an important issue to increase the system-level energy harvesting efficiency. Commonly used MPPT algorithms include perturb and observation (P&O) [5], incremental conductance [20], fractional open-circuit voltage (FOCV) and fractional short-circuit current (FSSC) [2]. However, most algorithms target conventional flat PV-cells because there is no analytical model that considers flexible PV-cells. MPPT algorithms for flexible PV-cells are proposed in [13, 23] to follow the global maximum power point. Chaotic-search and particle swarm optimization based MPPT algorithm is proposed due to absence of analytical model [13]. In addition, these algorithms are not suitable for wearable system due to their heavy computation cost. An MPPT algorithm that that target flexible PV-cells is proposed in [23]. This approach first approximates the location of global MPP using a fill factor model. Then, it employs a P&O algorithm to track the MPP. The method discussed in the paper fails to predict the exact location of global MPP. It is also unable to predict the MPP, if the degree of bending changes dynamically. Therefore, it is not suitable for IoT applications.

To the best of our knowledge, this is the first study to model the radiation and generated power as a function of bending of flexible PV-cells. We note that the proposed model can be used in conjunction with any existing MPPT algorithm, since this paper mainly focuses on analytical modeling of flexible PV-cells considering bending effects.

3 BENDING-AWARE RADIATION CHANGES IN A FLEXIBLE PV-CELL

A PV-cell generates power as a function of radiation intensity from the light source. Therefore, this section first presents a radiation model for flexible PV-cells by considering the bending radius. Then, we enhance the proposed model to account for partial shading that significantly affects the amount of generated power. Finally, we combine the proposed radiation model with a single diode equivalent circuit model to practically estimate the amount of generated power on multiple flexible PV-cells connected in series. The proposed model is used to estimate the harvested power and the MPP under different bending conditions. The goal of our modeling effort is to minimize the error between the estimated and actual values. The accuracy of the model is validated by the experiments presented in Section 4.

3.1 Analytical Radiation Model with Bending

3.1.1 Model Construction. Figure 3 illustrates the geometry of a flexible PV-cell, when it is flat (dashed line) or bent with the radius of curvature R (solid line). The first quantity of interest is the incident angle between the PV-cell surface and the rays from the light source. For a clear definition, we divide this angle into two components: elevation angle α and inclination angle β

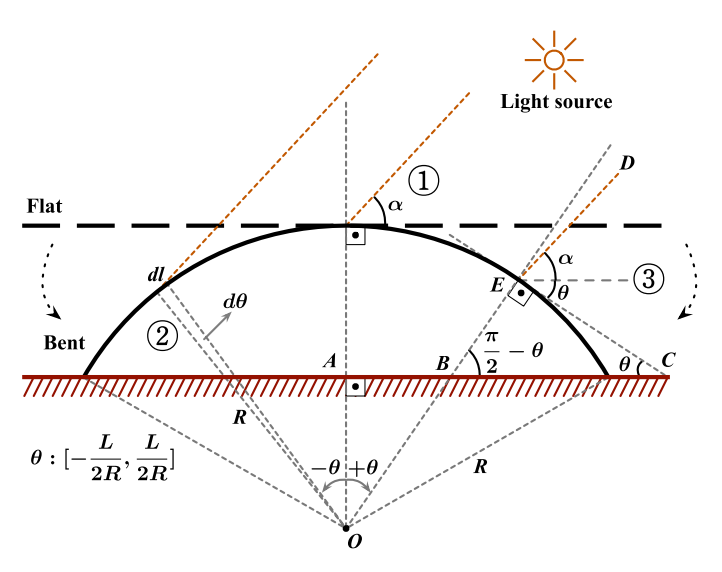


Fig. 3. Illustration of bending and major parameters.

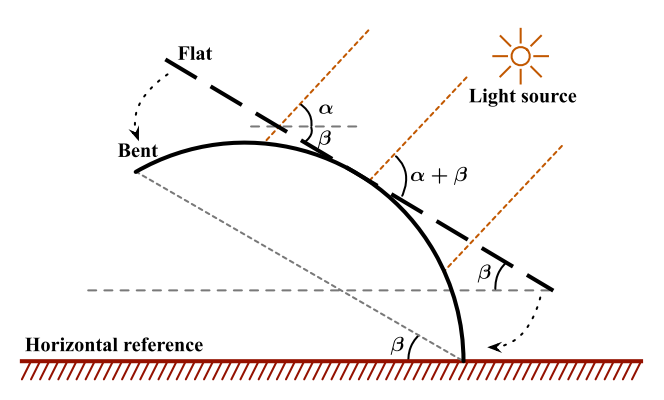


Fig. 4. Illustration of the inclination angle.

(where $0 \le \alpha, \beta \le \pi$) of the flat cell. The first term indicates the angle of light source from the ground surface as marked with ① in Figure 3, while the second term indicates the inclination angle of the PV-cell from the ground surface. For clarity, the flat PV-cell is plotted parallel to the ground in Figure 3, i.e., the inclination angle $\beta = 0$. A more general illustration is depited in Figure 4.

The amount of radiation received by the PV-cell is equal to the radiation intensity G, when the light rays are orthogonal to the PV-cell surface. However, if the light source has an elevation angle α or the PV-cell has an inclination angle β , the radiation at the PV-cell surface can be expressed as:

$$\lambda = \int_{-\frac{L}{2}}^{\frac{L}{2}} \int_{0}^{W} G \cdot \sin(\alpha + \beta) \ dwdl \tag{1}$$

where L and W indicate the length and the width of the PV-cell, respectively [3]. For simplicity, we only consider α and β where $0 \le \alpha, \beta \le \frac{\pi}{2}$ because sin function in the interval $\left[\frac{\pi}{2}, \pi\right]$ is symmetric with that of $\left[0, \frac{\pi}{2}\right]$. Since the radiation intensity, elevation and inclination angles are

156:6 J. Park et al.

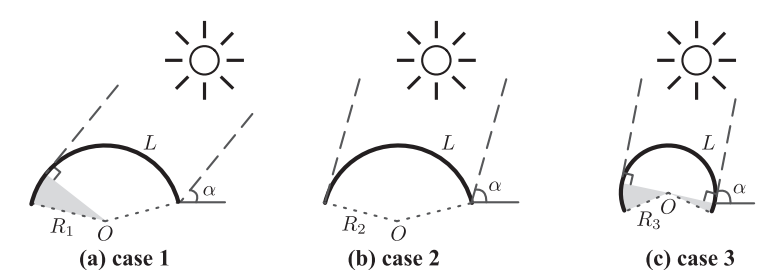


Fig. 5. Potential partial shading scenarios as a function of the ratio of the length of PV-cell to the radius of curvature and elevation angle. Note that $R_1 \neq R_2 \neq R_3$.

constant across the flat PV-cell, the amount of radiation can be found as follows:

$$\lambda_{flat} = L \cdot W \cdot G \cdot \sin(\alpha + \beta) \tag{2}$$

Unlike a flat PV-cell, the radiation at each infinitesimal point of a flexible PV-cell is *not* uniform. In what follows, we analyze the effective radiation changes with bending step by step.

When a PV-cell is bent with a radius of curvature R, it can be considered as an arc. The central angle of this arc is L/R. The length of an infinitesimal cross section of the arc, dl, can be expressed as $R \cdot d\theta$, where $d\theta$ is the corresponding infinitesimal angle. This is illustrated by the region marked with ② in Figure 3. By convention, we measure θ starting from the center, extending to either sides of the arc, i.e., $+\theta$ and $-\theta$. Hence, the limits of θ can be found as follows:

$$-\frac{L}{2} = R \cdot \theta_{min} \implies \theta_{min} = \frac{-L}{2R}, \qquad \frac{L}{2} = R \cdot \theta_{max} \implies \theta_{max} = \frac{L}{2R}$$

The final step in transforming Equation (1) is finding the angle between the incident light and the surface of the bent PV-cell as a function of θ . Note that the infinitesimal cross section at $\theta=0$ coincides with the flat position. Consider the triangle $\triangle OAB$ formed for an arbitrary $\theta>0$. We can easily see that $\angle B=\pi/2-\theta$, and $\angle C=\theta$ in Figure 3. The elevation angle α becomes an independent parameter as the distance between the PV-cell and light source increases. Therefore, the incident angle of the bent PV-cell at a specific infinitesimal point is found as $\angle DEC=\alpha+\theta$ which is marked with ③ in Figure 3. Hence, the total radiation received by the bent PV-cell can be found as follows:

$$\lambda_{bent} = \int_{\frac{-L}{2R}}^{\frac{L}{2R}} R \int_{0}^{W} G \cdot \sin(\alpha + \beta + \theta) \ dw d\theta \tag{3}$$

3.1.2 Derivation of the Analytical Model. Depending on the degree of bending, parts of the PV-cell can be shaded from the light source. Figure 5 illustrates three possible partial shading cases of a bent PV-cell depending on the L/R, α and β . We differentiate the radii of curvature using different symbols (R_1 , R_2 , R_3) in the figure and the subsequent analysis to explicitly show that the degree of bending is different in each case.

Case 1: Single-side shading $(\alpha + \beta - \frac{L}{2R_1} < 0)$

Unlike a flat PV-cell, shading happens as the PV-cell is bent (i.e., L/R_1 increases) and α approaches 0°. For example, some areas on the left side of the PV-cell can be shaded as illustrated in Figure 5(a), when the incident angle is less than 0° (i.e., $\alpha + \beta - \frac{L}{2R_1} < 0$). Since the shaded area does not contribute to power generation, we change θ_{min} from $\frac{-L}{2R_1}$ to $-(\alpha + \beta)$. Hence Equation (3)

is modified as follows:

$$\lambda_{bent,1} = \int_{-(\alpha+\beta)}^{\frac{L}{2R_1}} R_1 \int_0^W G \cdot \sin(\alpha+\beta+\theta) \, dw d\theta$$

$$= W \cdot G \cdot R_1 \left(1 - \cos\left(\alpha+\beta + \frac{L}{2R_1}\right)\right)$$
(4)

Note that, when the left side is shaded, we do not need to adjust θ_{max} , since the right side of the PV-cell is not affected. When only the right side is shaded, the analysis is symmetrical to the left side shading.

Case 2: No shading
$$(\alpha + \beta - \frac{L}{2R_2} \ge 0 \text{ and } \alpha + \beta + \frac{L}{2R_2} < \pi)$$

Case 2: No shading $(\alpha + \beta - \frac{L}{2R_2} \ge 0 \text{ and } \alpha + \beta + \frac{L}{2R_2} < \pi)$ In this condition, there will be no shaded area in both sides of the PV-cell, as shown in Figure 5(b). Thus, there is no need to adjust θ_{min} and θ_{max} . Hence, Equation (3) is the no shading case and is expressed as follows:

$$\lambda_{bent,2} = \int_{\frac{L}{2R_2}}^{\frac{L}{2R_2}} R_2 \int_0^W G \cdot \sin(\alpha + \beta + \theta) \, dw d\theta$$

$$= W \cdot G \cdot R_2 \left(\cos \left(\alpha + \beta - \frac{L}{2R_2} \right) - \cos \left(\alpha + \beta + \frac{L}{2R_2} \right) \right)$$

$$= 2W \cdot G \cdot R_2 \cdot \sin(\alpha + \beta) \sin \left(\frac{L}{2R_2} \right)$$
(5)

If R_2 is infinite, the equation should be the same as that of the flat PV-cell. Since $\lim_{R_2\to\infty} 2R_2$. $sin(L/(2R_2)) = L$ by L'Hopital's Rule, $\lim_{R_2 \to \infty} \lambda_{bent,2} = L \cdot W \cdot G \cdot sin(\alpha + \beta)$, which reduces to Equation (2).

Case 3: Both side shading
$$(\alpha + \beta + \frac{L}{2R_3} \ge \pi \text{ and } \alpha + \beta - \frac{L}{2R_3} < 0)$$

Both sides of the PV-cell may be shaded, when the flexible PV-cell is severely bent (L/R) is larger than π). In this case, the flexible PV-cell has shaded areas on both sides as illustrated in Figure 5(c). Therefore, both θ_{min} and θ_{max} should be adjusted in order to exclude the negative radiation integration due to the shaded areas. When both sides are shaded, Equation (3) is can be written as follows:

$$\lambda_{bent,3} = \int_{-(\alpha+\beta)}^{\pi-(\alpha+\beta)} R_3 \int_0^W G \cdot \sin(\alpha+\beta+\theta) \ dw d\theta$$

$$= 2W \cdot G \cdot R_2$$
(6)

Modeling the Impact of Partial Shading

In general, the open-circuit voltage of a single PV-cell is less than 1 V. Moreover, a single cell generates $10 - 20 \text{ mA/cm}^2$ current at 1000 W/m^2 [26]. Therefore, multiple PV-cells are connected in parallel to improve the current driving capability. Similarly, a set of PV-cells are connected in series to increase the output voltage. This resulting structure is called a PV-string. When one part of the PV-string falls under shade, the shaded cells start acting as power consumers instead of contributing to the generated power. This phenomenon, known as partial shading, has a significant impact on the harvested energy [31]. Therefore, it is crucial to account for partial shading problem when modeling the impact of bending on flexible PV-cells.

Radiation intensity at each infinitesimal point on a flexible PV-string is different when it is bent, as shown in Section 3.1. Since each infinitesimal point may belong to a different PV-cell, a subset of cells (more than one PV-cell) may be under the shade together. Therefore, the contribution of 156:8 J. Park et al.

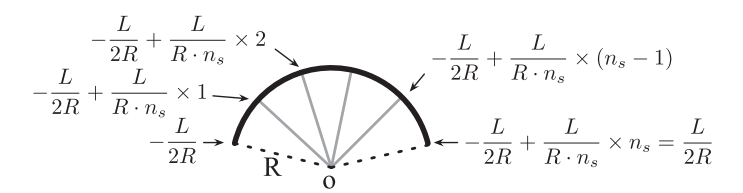


Fig. 6. A flexible PV-string diagram for a partial shading.

each cell needs to be accounted individually to obtain accurate results. To this end, we refine our proposed flexible PV-cell model by explicitly dividing the whole PV-string into multiple PV-cells. As an example, Figure 6 shows a PV-string with a length of L, consisting of n_s cells. When this PV-string is bent with a radius of curvature R, each cell forms an arc with a length of $L/(R \cdot n_s)$.

We note that Equation (3) gives the radiation on a *single* flexible PV-cell of length L with a radius of curvature R. When a series of n_s PV-cells are connected to form a string, we use this equation to express the total radiation of the i^{th} PV-cell in a PV-string as follows:

$$\lambda_{i} = \int_{\frac{-L}{2R} + \frac{L \cdot i}{R \cdot n_{s}}}^{\frac{-L}{2R} + \frac{L \cdot i}{R \cdot n_{s}}} R \int_{0}^{W} G \cdot \sin(\alpha + \beta + \theta) \ dw d\theta, \tag{7}$$

where $1 \le i \le n_s$. The bounds of the first integral are set according to Figure 6. For example, the range of θ for i^{th} segment is defined from $\frac{-L}{2R} + \frac{L \cdot (i-1)}{R \cdot n_s}$ to $\frac{-L}{2R} + \frac{L \cdot i}{R \cdot n_s}$. Note that the i^{th} PV-cell belongs to one of three cases described in Section 3.1. Therefore, we evaluate Equation (7) to generalize our model to PV-strings by leveraging the radiation models summarized in Equations (4)–(6). In particular, *each PV-cell* falls into one of the following four categories.

I. A given PV-cell is completely under shade: This happens if even the upper limit of the integral is negative, or if even the lower limit is smaller than π . More precisely:

$$\alpha + \beta - \frac{L}{2R} + \frac{L \cdot i}{R \cdot n_s} < 0 \quad OR \quad \alpha + \beta - \frac{L}{2R} + \frac{L \cdot (i-1)}{R \cdot n_s} \ge \pi$$

If any one of these two conditions is true, the corresponding PV-cell is completely under shade. Therefore, the radiation should be zero.

II. Part of the PV-cell is under shade: In this scenario, the left or right side of the PV-cell is under shade, while the remaining part receives light. Since this scenario coincides with Case 1 studied in Section 3.1, we leverage Equation (4) by refining the limits of the integral. When the left part is shaded, we have:

Condition:
$$\alpha + \beta - \frac{L}{2R} + \frac{L \cdot (i-1)}{R \cdot n_s} < 0$$
 AND $\alpha + \beta - \frac{L}{2R} + \frac{L \cdot i}{R \cdot n_s} \ge 0$

$$\lambda_i = W \cdot G \cdot R \left(1 - \cos \left(\alpha + \beta - \frac{L}{2R} + \frac{L \cdot i}{R \cdot n_s} \right) \right)$$
(8)

When the right part of the PV-cell is shaded, we have:

Condition:
$$\alpha + \beta - \frac{L}{2R} + \frac{L \cdot (i-1)}{R \cdot n_s} < \pi \quad AND \quad \alpha + \beta - \frac{L}{2R} + \frac{L \cdot i}{R \cdot n_s} \ge \pi$$

$$\lambda_i = W \cdot G \cdot R \left(1 + \cos \left(\alpha + \beta - \frac{L}{2R} + \frac{L \cdot (i-1)}{R \cdot n_s} \right) \right) \tag{9}$$

III. The PV-cell does not fall under shade: In this scenario, the whole cell receives light. Since this scenario coincides with Case 2 studied in Section 3.1, we leverage Equation (5) by refining the

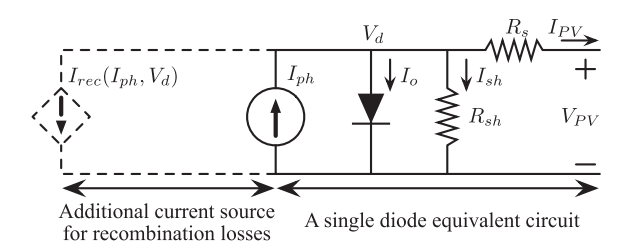


Fig. 7. A single diode equivalent circuit model considering recombination losses.

limits of the integral. Hence, we have:

$$Condition: \alpha + \beta - \frac{L}{2R} + \frac{L \cdot (i-1)}{R \cdot n_s} \ge 0 \quad AND \quad \alpha + \beta - \frac{L}{2R} + \frac{L \cdot i}{R \cdot n_s} < \pi$$

$$\lambda_i = W \cdot G \cdot R \left(\cos \left(\alpha + \beta - \frac{L}{2R} + \frac{L \cdot (i-1)}{R \cdot n_s} \right) - \cos \left(\alpha + \beta - \frac{L}{2R} + \frac{L \cdot i}{R \cdot n_s} \right) \right)$$
(10)

IV. Both sides of the PV-cell have shade: This is an extreme scenario, which can happen if the radius of curvature is comparable the length of a single cell. This scenario coincides with Case 3 studied in Section 3.1. Therefore, we leverage Equation (6) by refining the limits of the integral to obtain:

Condition:
$$\alpha + \beta - \frac{L}{2R} + \frac{L \cdot (i-1)}{R \cdot n_s} < 0$$
 AND $\alpha + \beta - \frac{L}{2R} + \frac{L \cdot i}{R \cdot n_s} \ge \pi$

$$\lambda_i = 2W \cdot G \cdot R \tag{11}$$

3.3 Current-Voltage Modeling of PV-cells

This section explains how we apply the radiation models derived in Section 3.1 and Section 3.2 to a concrete PV-cell model.

PV-cell characterization: The I-V curve of a PV-cell is commonly modeled using a single diode equivalent circuit shown Figure 7 (without the current source shown using dotted lines). This circuit consists of a photo current source I_{ph} , a diode with saturation current I_o , a series resistor R_s and a shunt resistor R_{sh} . A single diode circuit models crystalline PV-cells accurately, but it fails to capture the behavior of amorphous PV-cells [15, 16] targeted in this work. In amorphous PV-cells, the recombination losses in the intrinsic layer affect the output current. Therefore, we employ the equivalent circuit with an additional current source I_{rec} , as shown in Figure 7 [16]. Thus, the output current I_{PV} of this circuit can be expressed as follows:

$$I_{PV} = I_{ph} \cdot \left(1 - \frac{d_I^2}{\mu \tau_{eff}(V_{bi} - V_d)} \right) - I_o \left(e^{\frac{V_d}{A \cdot V_t}} - 1 \right) - \frac{V_d}{R_{sh}}$$
 (12)

where d_I , $\mu \tau_{eff}$, V_{bi} , V_d , V_t and A are the thickness of the intrinsic layer, effective diffusion length of the charge carrier, built-in voltage, diode voltage, thermal voltage, and diode ideality factor, respectively.

Thorough empirical measurements under different bending conditions (detailed in Section 4) show that I_{ph} , R_{sh} and I_o depend on the radiation λ , which is in agreement with the literature [4, 16]. More specifically, R_{sh} increases as λ decreases, while I_o increases with λ . Similar to existing

156:10 J. Park et al.

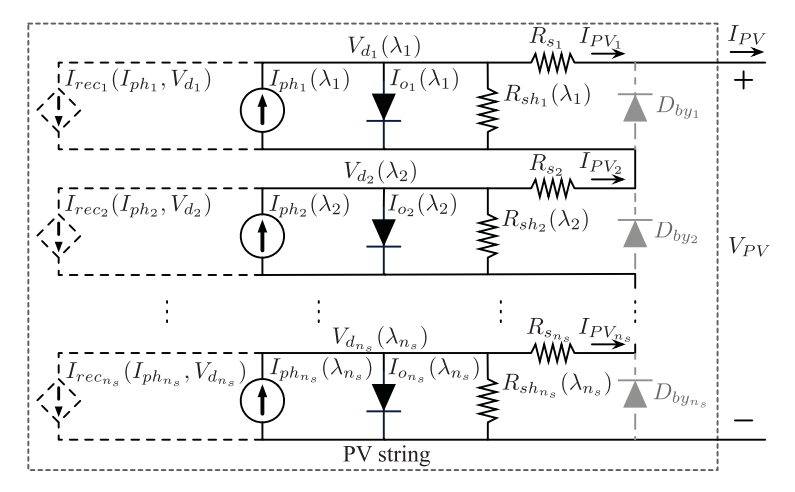


Fig. 8. An equivalent circuit model for a PV-string.

research [4, 16], we model I_{ph} , R_{sh} , and I_o as functions of λ as follows:

$$I_{ph} = a_{IPH} \cdot \left(\frac{\lambda}{W \cdot L}\right)^{b_{IPH}},$$

$$I_{o} = a_{IO} \cdot \left(\frac{\lambda}{W \cdot L}\right)^{2} + b_{IO} \cdot \frac{\lambda}{W \cdot L} + c_{IO},$$

$$R_{sh} = a_{RSH} \cdot e^{b_{RSH} \cdot \frac{\lambda}{W \cdot L}}$$
(13)

where a_{IPH} , b_{IPH} , a_{IO} , b_{IO} , c_{IO} , a_{RSH} , and b_{RSH} are unknown modeling parameters. As it is commonly done, we use measured I-V data at a wide range of radiation intensities, and find these coefficients through least squares minimization.

From PV-cell to PV-string: A PV-string exposed to uneven radiation cannot be modeled as a single diode equivalent circuit because PV-cells with different radiation behavior differently. We refine the model as a circuit that consists of multiple single diode equivalent circuits connected in series as shown in Figure 8 [31]. In this case, current through the i^{th} PV-cell I_{PV_i} can be expressed as:

$$I_{PV_{i}} = I_{ph_{i}} \cdot \left(1 - \frac{d_{I}^{2}}{\mu \tau_{eff}\left(\frac{V_{bi}}{n_{s}} - V_{d_{i}}\right)}\right) - I_{o_{i}}\left(e^{\frac{V_{d_{i}}}{A \cdot V_{I}}} - 1\right) - \frac{V_{d_{i}}}{R_{sh_{i}}}$$

$$I_{ph_{i}} = a_{IPH} \cdot \left(\frac{\lambda_{i}}{W \cdot \left(\frac{L}{n_{s}}\right)}\right)^{b_{IPH}},$$

$$V_{d_{i}} = V_{PV_{i}} + I_{PV_{i}} \cdot R_{s_{i}},$$

$$I_{o_{i}} = a_{IO} \cdot \left(\frac{\lambda_{i}}{W \cdot \left(\frac{L}{n_{s}}\right)}\right)^{2} + b_{IO} \cdot \left(\frac{\lambda_{i}}{W \cdot \left(\frac{L}{n_{s}}\right)}\right) + c_{IO},$$

$$R_{s_{i}} = R_{s}/n_{s},$$

$$R_{sh_{i}} = \frac{a_{RSH}}{n_{s}} \cdot e^{b_{RSH} \cdot \left(\frac{\lambda_{i}}{W \cdot \left(\frac{L}{n_{s}}\right)}\right)}$$

$$(14)$$

where V_{PV_i} is i^{th} PV-cell voltage. Note that the model parameters (a_{IPH} , b_{IPH} , a_{IO} , b_{IO} , c_{IO} , a_{RSH} , and b_{RSH}) are found during PV-cell characterization. Furthermore, radiation under bending λ_i is calculated using Equations (7) through (11). Therefore, we can compute I_{PV_i} , I_{o_i} and R_{sh_i} for each

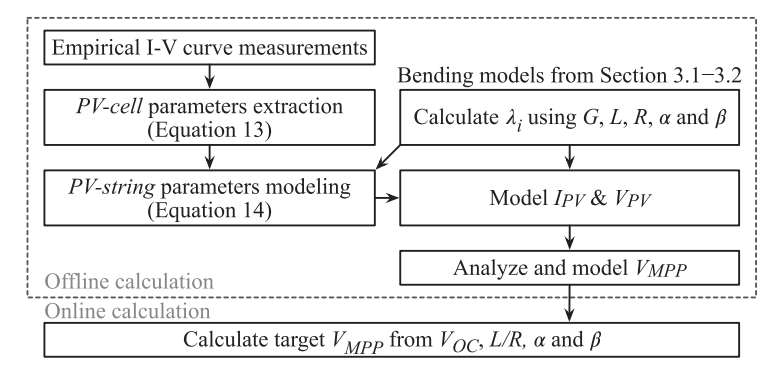


Fig. 9. An example flow chart from I-V modeling of the flexible PV-cell to MPPT algorithm implementation.

cell in the string. It remains to calculate I_{PV} and V_{PV} by using the equivalent circuit depicted in Figure 8.

As shown in Figure 2, bending a PV-string reduces the output power significantly, and can cause hotspots. Designers may use bypass diodes to alleviate this drawback. A bypass diode is located in parallel with a PV-cell, as shown in Figure 8. The existence of bypass diodes determines the equation to calculate I_{PV} and V_{PV} .

Without the bypass diodes: If there are no bypass diodes, I_{PV_i} is equal to I_{PV} because PV-cells are connected in series. Therefore, I_{PV} and V_{PV} are calculated by solving the following equation:

$$I_{PV} = I_{PV_1} = I_{PV_2} = \dots = I_{PV_{n_s}}.$$
 (15)

With the bypass diodes: If there are bypass diodes, the current of the i^{th} bypass diode is denoted by I_{D_i} . Then, we have:

$$I_{PV} = I_{PV_1} + I_{D_1} = I_{PV_2} + I_{D_2} = \dots = I_{PV_{n_s}} + I_{D_{n_s}}$$
(16)

Hence, I_{PV} and V_{PV} are calculated by solving Equation (16). Note that bypass diodes may introduce local MPPs. Since λ_i is independent of bypass diodes, we are able to estimate the effect of bypass diodes and find local MPPs.

Summary and Application to MPPT: In summary, we start with a characterization of the target PV-cell by measuring the I-V curve for different radiation intensities. Then, this model is used to extract the PV-cell parameters (Equation (13)), as shown in Figure 9. The characterized PV-cell parameters and our radiation models are used together to find the current and voltage of a PV-string by solving Equation (14)–(16). We emphasize that these calculations are performed only once. Then, the extracted parameters are used to compute the I-V curve of the PV-string.

For MPPT algorithms, we only need to model the maximum voltage point V_{MPP} as a function of bending. For example, the FOCV algorithm needs only V_{MPP}/V_{OC} . Therefore, we derive an expression for V_{MPP}/V_{OC} as a function of L/R and elevation angle α , as illustrated in Section 4.4. At runtime, we only evaluate this expression with 277.8 μ s computation overhead. The validation of our approach using a commercial PV-string, and application scenario and overhead analysis are described in the following section.

4 EXPERIMENTAL RESULTS

4.1 Experimental Setup

We validate the proposed analytical models using our custom-built experimental setup shown in Figure 10. The radiation intensity is controlled using a halogen lamp and a solar power meter TES

156:12 J. Park et al.

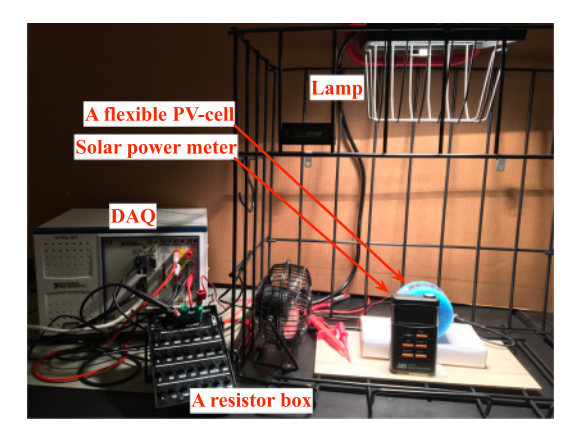


Fig. 10. Experimental setup to measure the generated power from a commercial flexible PV-cell.

Parameter	Value	Parameter	Value
a_{IPH}	1.077E-7	R_s	75 Ω
b_{IPH}	1.489	A	4.2
a_{IO}	-3.103E-13	$d_I^2/\mu au_{e\!f\!f}$	0.003
b_{IO}	1.118E-9	V_{bi}	0.9V
c_{IO}	3.776E-8	n_s	5
a_{RSH}	5.426E+5	L	50.8~mm
b_{RSH}	-3.687E-3	W	$12.7 \ mm$

Table 1. Extracted PV Parameters

1333 [28], while the load is adjusted using a resistor box. We minimize the time that PV-cell is exposed under the light to maintain the temperature of PV-cell constant. Moreover, we allocate sufficient time between different experiments to let the PV-cell cool down to ensure controllable experiments, i.e., obtain repeatable results. Finally, we measure the output voltage and current of the PV-cell using NI PXIe-4081 [18] and PXIe-4080 [17]. We employ rectangular FlexSolarCell PV SP3-12 unit [6] in our experiments. It is attached to the lateral surface of a cylindrical foam with a given radius of curvature R to control bending. We rotate the cylindrical foam to emulate the change in the elevation angle α .

In our experiments, we sweep the PV-cell voltage with the help of a resistor box with 1Ω resolution. The load resistance is adjusted to achieve a voltage resolution less than 0.3 V. For each setting, we perform three measurements at each voltage to obtain consistent readings. Finally, we upsample the measured data by 100 to obtain better accuracy when extracting the circuit parameters. The extracted PV-cell parameters used in this work are listed in Table 1.

In what follows, we first describe how the PV-cell parameters are extracted using the proposed models and validated empirically. Then, we show that the flexible PV-cell models are able to boost the harvested energy, and compare the accuracy of our approach against the model presented in [23]. Finally, we discuss the runtime overhead of utilizing the proposed flexible PV-cell models.

4.2 Extraction of the Flat PV-cell Parameters

The first step towards validating the proposed analytical models is to extract the parameters of the PV-cell given in Equation (12). We measure the I-V characteristics of the flat PV-cell for radiation intensities ranging from 100 to 1000 W/m^2 , in increments of 100 W/m^2 , while keeping α fixed

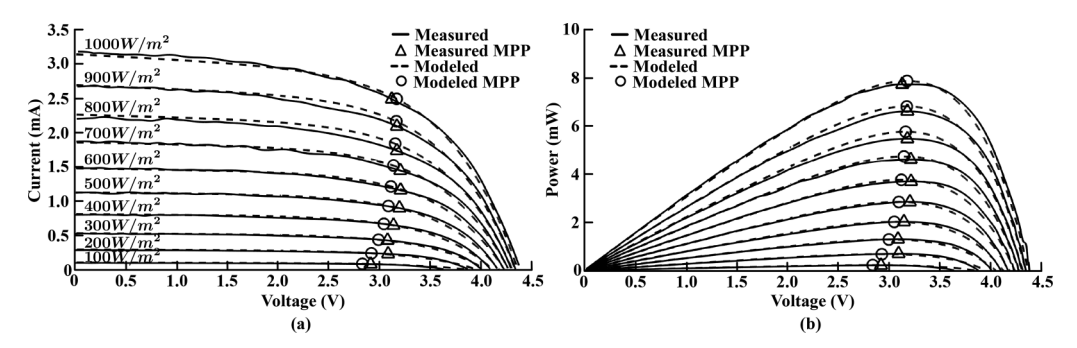


Fig. 11. Comparison of measurement and modeling results for (a) current and (b) power for a flat PV-cell.

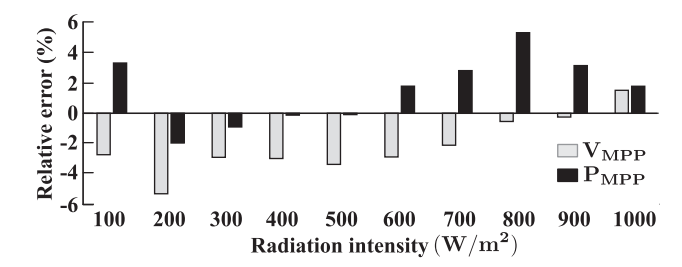


Fig. 12. Relative error of modeled V_{MPP} and P_{MPP} against measured data for flat PV-cells.

at 90°. Then, we extract initial values of parameters in Equation (12) at each intensity without accounting for the recombination losses [21]. The recombination losses affect current degradation near the MPP. So, we estimate the initial value of $d_I^2/\mu\tau_{eff}$ by comparing current around the MPP. Then, we repeat the parameter extraction using these values, and continue this iteration until the parameters converged. Finally, we extract the I_{ph} , I_o and R_{sh} parameters summarized in Table 1.

Figure 11(a) and Figure 11(b) compare the measured data (solid line) against the modeling results (dashed line) for the flat PV-cell as the radiation intensity ranges from 100 to 1000 W/m^2 . We observe a good fit across the feasible voltage range. The normalized root mean square error (NRMSE) of power obtained from our model is 1.8%.

The most critical point on the P-V curve is the MPP, because it maximizes the harvested energy. \triangle and \circ markers in Figure 11(a) and Figure 11(b) show the measured MPP and the modeling results, respectively. The predicted MPP voltage, V_{MPP} , matches very well with the measured voltage, as shown in Figure 12. The relative percentage error is less than 6%. The harvested power at the MPP, P_{MPP} , also exhibits low prediction error, as shown in Figure 12. In particular, the average error is less than 3% across the range of radiation intensities, and the maximum error is 5.3%.

4.3 Validation of the Flexible PV-Cell Model

After confirming the accuracy of the flat PV-cell model, we validate the flexibility models presented in Section 3 by computing the effective radiation intensity under different scenarios. More precisely, we evaluate our models for three cases: (1) Flat PV-string as a baseline, (2) PV-string bent with a radius of curvature $R = 40 \, mm$ without considering partial shading, (3) and $R = 40 \, mm$ but by considering partial shading.

Figure 13(a) shows the estimated and measured power generation as a function of the PV-cell voltage when the elevation angle $\alpha = 90^{\circ}$. We observe that there is a very good match between

156:14 J. Park et al.

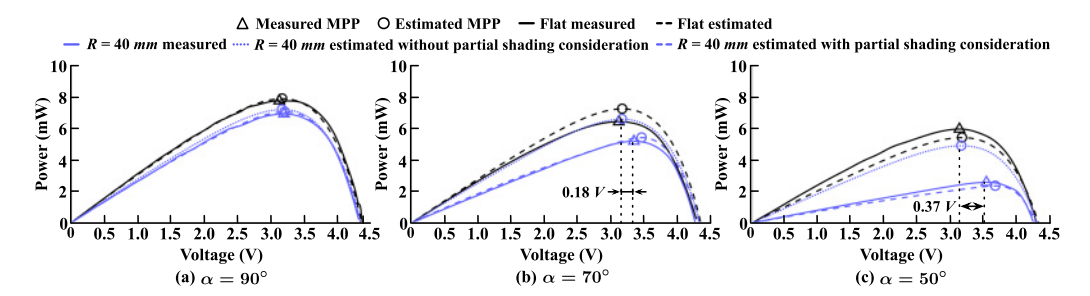


Fig. 13. Comparison of measured data and estimated data for $G = 1000 W/m^2$.

		33711		. 1 1	1.	• 1		33711		1 1 1		• 1	
		With	Without partial shading consideration			With partial shading consideration							
		V_{MPP} (%)		P_{MPP} (%)		V_{MPP} (%)		P_{MPP} (%)					
	Elevation angle	90°	70°	50°	90°	70°	50°	90°	70°	50°	90°	70°	50°
	1000	-0.8	-5.3	-10.6	4.0	27.0	90.0	0.4	3.6	3.9	1.9	4.4	-8.8
ify	900	-0.8	-5.9	-10.3	4.8	26.5	89.5	0.5	3.0	4.2	2.5	3.4	-9.6
Intensity (W/m^2)	800	-1.5	-7.4	-13.8	3.9	27.1	99.5	-0.1	1.4	-0.1	1.6	3.4	-5.3
	700	-1.2	-7.0	-12.4	5.6	27.2	93.7	0.2	1.9	1.3	3.1	3.1	-8.4
Ι	600	-27	-5.8	_117	5.5	27.4	20 Q	-14	3 2	2.1	3.0	3.0	-10.5

Table 2. Estimation Error Compared to Measured Data at R = 40 mm

the modeling result and measured data for all three cases. In particular, the error in the V_{MPP} and P_{MPP} estimates are less than 3%, as summarized in Table 2. Since partial shading is negligible when $\alpha=90^\circ$, the model that *does not* consider partial shading still works well. This observation is supported by Figure 13(b), which shows the measured and analysis results for $\alpha=70^\circ$. The V_{MPP} and P_{MPP} estimation error jump to 7.5% and 27.4%, when partial shading is not considered. In contrast, our model that takes partial shading into account results in only 3.6% and 4.4% error in predicting the V_{MPP} and P_{MPP} , as summarized in Table 2. The same observation holds when the elevation angle is further reduced to $\alpha=50^\circ$. Our models, which consider partial shading, keep up very well with the measured data. However, ignoring partial shading leads to as high as 13.8% error in the V_{MPP} and 99.5% error in P_{MPP} estimation. In contrast, the proposed analytical models give very good accuracy across a wide range of intensities, as summarized Table 2.

Having established the accuracy of the proposed analytical models, we present next an MPPT case study that demonstrates the benefits of the proposed models.

4.4 Boosting Energy Harvesting for MPPT using Flexible PV-Cell Models

It is well-known that the ratio between V_{MPP} and the open circuit voltage V_{OC} (V_{MPP}/V_{OC}) does not vary significantly with radiation intensity. Fractional open-circuit voltages, i.e., FOCV, MPPT algorithm utilizes this information to track the maximum power point V_{MPP} . FOCV can be implemented with a small overhead by forming a voltage divider using resistors. Hence, it is very practical and suitable for wearable IoT applications. Indeed, commercial chargers adopt the FOCV algorithm to support MPPT [29].

Impact of Bending on V_{MPP}/V_{OC} : Bending results in uneven radiation on a flexible PV-cell, which affects the maximum power point, as described in Section 4.3. To analyze the impact of bending on the FOCV algorithm, we analyze the V_{MPP}/V_{OC} ratio under different bending scenarios

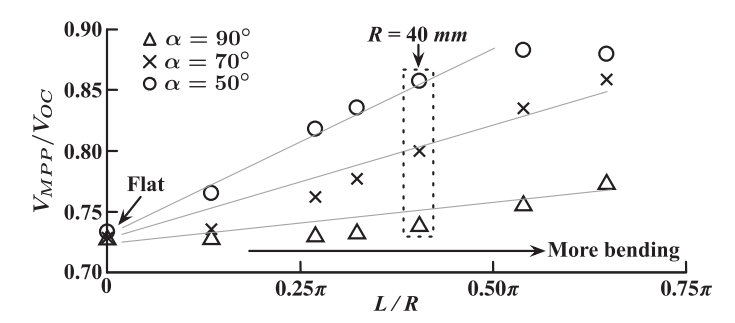


Fig. 14. V_{MPP}/V_{OC} changes according to L/R change.

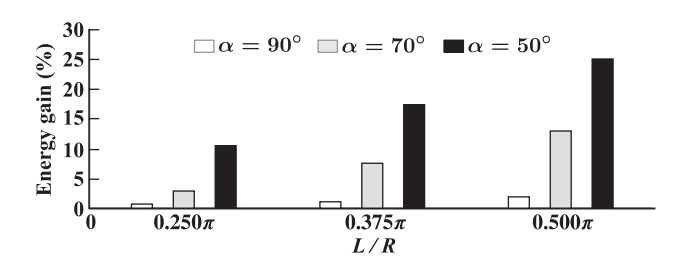


Fig. 15. Comparison of energy gain according to L/R ratio.

using the proposed analytical models. The degree of bending is quantified using the L/R ratio, where L/R = 0 ($R \to \infty$) corresponds to a flat PV-cell and $L/R = 0.5\pi$, meaning a quarter of circle. Figure 14 plots V_{MPP}/V_{OC} as a function of bending for different elevation angles. First, we ob-

Figure 14 plots V_{MPP}/V_{OC} as a function of bending for different elevation angles. First, we observe that V_{MPP}/V_{OC} remains constant for a flat PV-cell (L/R=0) regardless of the elevation angle. This observation aligns with the basic assumption of FOCV. Second, Figure 14 shows that V_{MPP}/V_{OC} increases linearly with bending, i.e., when the radius of curvature R becomes smaller. Furthermore, the rate of increase is a function of the elevation angle α . Large amounts of bending and low α imply that the PV-cell suffers more from a partial shading. At $\alpha=50^\circ$, the value of upper right point stops increasing even though it is bent more. This happens when shading occurs on a flexible PV-cell. These results clearly show that a flexible PV-string cannot rely on constant V_{MPP}/V_{OC} values to track the maximum power point.

Harvested Energy Evaluation: We evaluate the energy harvested by the FOCV algorithm with and without the proposed models using a custom PV-string model and FOCV algorithm implemented in MATLAB Simulink. The simulated system consists of a flexible PV-cell, a charger with FOCV MPPT, a boost DC-DC converter and a lithium-ion battery. Our model uses the parameters of the commercial SP3-12 flexible PV-cell. Similarly, it adopts parameters for a charger from the commercial product [29]. The model has a lithium-ion battery which is a single cell with 50 mAh capacity. We compare the amount of energy harvested in a lithium-ion battery during a given time under different scenarios.

In our experiments, we evaluate the amount of harvested energy by varying the degree of bending $L/R \in 0.25\pi, 0.375\pi, 0.5\pi$ and the elevation angle $\alpha \in 50^\circ, 70^\circ, 90^\circ$. First, the harvested energy is found for each combination by using the baseline FOCV algorithm that uses a constant V_{MPP}/V_{OC} ratio. Then, the simulations are repeated by using the improved FOCV algorithm that predicts the V_{MPP}/V_{OC} ratio using the proposed models. Figure 15 shows the percentage increase in the harvested energy as a function of the elevation angle and bending. When the PV-string is

156:16 J. Park et al.

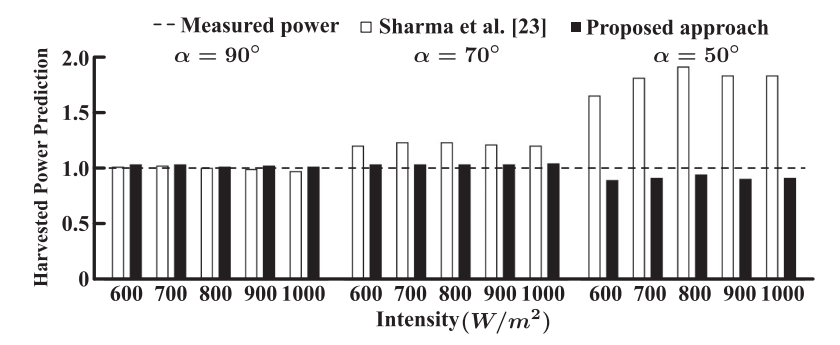


Fig. 16. Comparison of modeled P_{mpp} to measured value. Average relative error of the proposed model is 2.4%, 3.5%, and 8.5% when α is 90°, 70°, and 50°, respectively. In comparison, the average relative error of Sharma et al. [23] is 0.40%, 21.7%, and 81% when α is 90°, 70°, and 50°, respectively.

bent slightly ($L/R=0.25\pi$) and the elevation angle is 90°, we observe minor increase in the harvested energy. However, the harvested energy increases sharply both with the degree of bending and elevation angle. In particular, we achieve 10.5% harvested energy when only the elevation angle drops to 50°. When the PV-string is bent 50% more, i.e., L/R increases from 0.25π to 0.375π , the percentage savings increases to 17.4%. Finally, we harvest 25.0% larger energy for $\alpha=50^\circ$ and $L/R=0.5\pi$.

The improved FOCV algorithm is able to harvest more energy, since it can track the maximum power point very accurately. As a result, the improvement in the harvested energy becomes larger when there is larger variation in V_{MPP}/V_{OC} . Therefore, the improvement in the harvested energy is aligned with the V_{MPP}/V_{OC} variation shown in Figure 14.

4.5 Comparison with PV-Cell Model from [23]

This section compares the accuracy of the proposed model against the flexible PV-cell model presented in [23] both in terms of V_{MPP} and P_{MPP} prediction, and harvested energy.

Accuracy of V_{MPP} and P_{MPP} Prediction: The approach presented in [23] models the MPP of a flexible PV-cell using a short-circuit current, a open-circuit voltage and a fill factor when it is bent. For finding the coefficients used in the model, they perform experimental measurements for different bending. Then they perform regression analysis to fit the measurement to a nonlinear model. Unlike our technique, their approach requires different sets of measurements for each bending scenario.

Figure 16 compares the harvested power predicted by the approach in [23] and ours against the measured values. The coefficients used in [23] are extracted from the measurement at R=40~mm and $\alpha=90^\circ$. Note that our approach requires only PV parameters extracted from the measurements when a flexible PV-cell is flat. We observe that both approaches achieve very good accuracy (less than 2.4%), when the elevation angle is 90° . However, our approach performs significantly better as the elevation angle decreases. More precisely, the prediction error of our technique increases slightly to 3.5%, while the approach presented in [23] leads to 21.7% error. Similarly, the accuracy of our approach is significantly better (8.5% versus 81%) error, when the elevation angle is 50° . The accuracy of the technique presented in [23] decreases abruptly with lower elevation angles, since their model does not consider the angle between the PV-cell and the incident light.

Similarly, we compare the voltage at the MPP predicted by our approach and Sharma et al. [23] in Figure 17. Again, both approaches perform very well and lead to less than 2.0% error when the

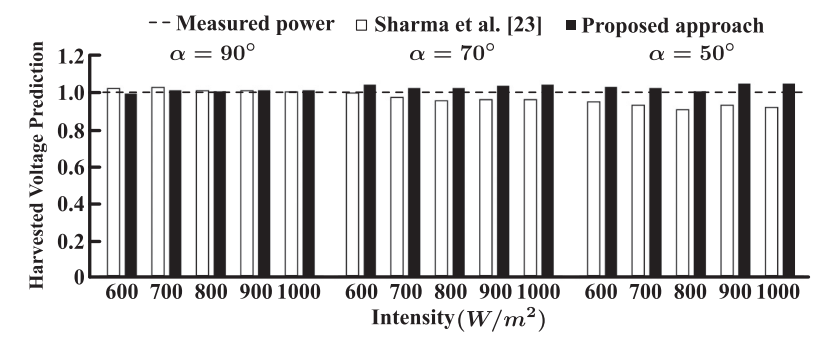


Fig. 17. Comparison of modeled V_{mpp} to measured value. Average relative error of the proposed model is -1.4%, -2.6%, and 2.9% when α is 90° , 70° , and 50° , respectively. In comparison, the average relative error of Sharma et al. [23] is 2.0%, -4.3%, and -7.7% when α is 90° , 70° , and 50° , respectively.

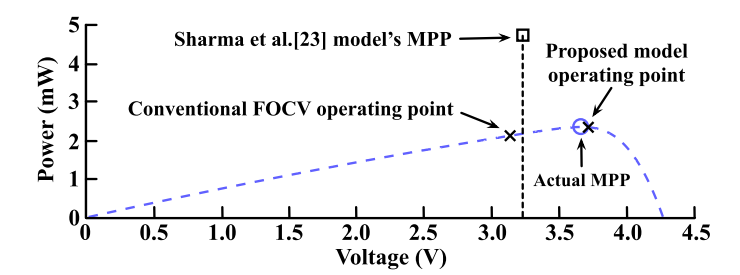


Fig. 18. Comparison of the operating point for $\alpha = 50^{\circ}$.

elevation angle is 90° . When the elevation angle decreases to 70° and 50° , the modeling error of our approach increases marginally to 2.6% and 2.9%, respectively. Under the same scenario, the accuracy of the approach presented in [23] increases to 4.3% and 7.7%, respectively.

Impact on the Harvested Energy: The accuracy of the flexible PV-cell model affects the harvested energy. We calculate V_{MPP}/V_{OC} using the proposed model and Sharma et al. [23] to compare them in terms of harvested energy using the same setup explained in Section 4.4. Note that the harvested energy is compared only when R=40 mm, the technique proposed in [23] requires new sets of measurements for different radius of curvature R. Since both approaches have high accuracy for $\alpha=90^\circ$, they lead to similar gains. Improved FOCV MPPT algorithm based on the proposed model achieves 8.8% and 18.8% with $\alpha=70^\circ$ and $\alpha=50^\circ$, respectively. However, the improved FOCV MPPT algorithm based on [23] achieving only 2.8%, and 4.6% more energy than the conventional FOCV MPPT algorithm when $\alpha=70^\circ$ and $\alpha=50^\circ$, respectively. Our approach leads to significantly larger harvested energy, since it can operate much closer to the MPP than both the convention FOCV and FOCV that utilizes the bending model from Sharma et al. [23], as illustrated in Figure 18.

4.6 Runtime Operation and Overhead Analysis

As stated in Section 1, we envision that the flexible PV-cells considered in this work will power wearable IoT devices [1]. For example, they can be attached to forearm, shoulder or to the chest. The flexibility ensures that the PV-cells can conform to the shape of the body. When the person moves, the inclination angle β or the radius of curvature R may change. Our model captures both of these parameters.

156:18 J. Park et al.

Parameter	Operation	Time	Period
R	Read a flex sensor	2.7 μs	100 ms
β	Compute β using accelerometer	570.7 μs	100 ms
α	Get time/location from BLE	2.4 ms	10 min
	Calculate α	1.0 ms	10 min
V_{OC}	Read V_{OC}	30.5 μs	100 ms
V_{MPP}	Compute and set V_{MPP}	277.8 μs	100 ms

Table 3. Runtime Operation and Overhead

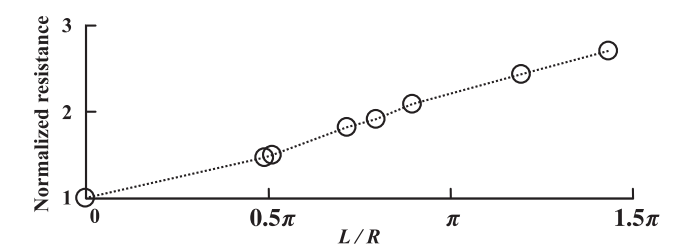


Fig. 19. Normalized resistance as a function of bending.

Minimizing the runtime overhead is important to run an MPPT algorithms on wearable devices. Therefore, we analyze the overhead of utilizing the proposed flexible PV-cell models in the improved FOCV MPPT algorithm. The proposed approach runs with a period of 100 ms to capture the parameter change due to the body movement. The sequence of operation required by our algorithm, its runtime and periodicity are summarized in Table 3. To compute the radius of curvature R, we employ flex sensor FS-L-0095-103-ST [27] which changes its resistance linearly according to L/R as shown in Figure 19. This operation takes only 2.7 μs to complete. Next, we sample a 3-axis accelerometer [8] to obtain the orientation of flexible PV-cell (β), with 570.7 μ s runtime overhead. The last external input to the proposed approach is the elevation angle of the sun α . Since it does not change rapidly unlike the other two, we can sample it with much longer intervals. More specifically, we use GPS data to find the current time and location every 10 min. Even if the wearable system does not have access to the GPS, it can receive this information from a nearby mobile device, such as a smartphone. The current time and location enable computing α using the equation that describes the Sun position in the sky [25]. The total communication and computation time is 2.4 ms, as shown in Table 3. Finally, reading V_{OC} and computing V_{MPP}/V_{OC} using the results of offline regression analysis take 30.5 μ s and 277.8 μ s, respectively.

In summary, the total computation overhead is less than 0.9 ms out of 100 ms (less than 1%), when the proposed approach is implemented with a TI's CC2650 processor which operates up to 48 MHz [30]. As the elevation angle of the Sun, i.e. α , changes slowly, there is an additional 1.0 ms overhead to update α every 10 min. Hence, the proposed model can boost the harvested energy in wearable IoT applications.

5 CONCLUSIONS

Energy harvesting is the one of most important problems in low power IoT devices. A flexible PV-cell can enable uninterrupted operation of wearable IoT devices. However, to date, there are

no analytical models that describe the impact of bending on the harvested energy and maximum power point. This paper studies the effect of bending on harvested energy both analytically and empirically. We show that bending can have a dramatic impact on the harvested energy, since it changes the radiation intensity and can lead to partial shading. Our analytical models estimate the voltage and power at the maximum power point within 4.2% and 10.5% accuracy compared to measured data on a commercial flexible PV-cell. Finally, we show that the proposed analytical model can lead up to 25.0% increase in harvested energy when used with MPPT algorithms.

REFERENCES

- [1] Ganapati Bhat, Jaehyun Park, and Umit Y. Ogras. 2017. Near optimal energy allocation for self-powered wearable systems. In *Proceedings of International Conference on Computer Aided Design*.
- [2] Davide Brunelli, Luca Benini, Clemens Moser, and Lothar Thiele. 2008. An efficient solar energy harvester for wireless sensor nodes. In *Proceedings of the Design, Automation and Test in Europe.* 104–109.
- [3] Christiana Honsberg and Stuart Bowden. 2017. Arbitrary Orientation and Tilt. http://www.pveducation.org/pvcdrom/arbitrary-orientation-and-tilt. (2017).
- [4] Widalys De Soto, S. A. Klein, and W. A. Beckman. 2006. Improvement and validation of a model for photovoltaic array performance. *Solar Energy* 80, 1 (2006), 78–88.
- [5] Mohammed A. Elgendy, Bashar Zahawi, and David J. Atkinson. 2012. Assessment of perturb and observe mppt algorithm implementation techniques for PV pumping applications. IEEE Transactions on Sustainable Energy 3, 1 (2012), 21–33.
- [6] FlexSolarCells. 2017. SP3-12 datasheet. http://www.flexsolarcells.com/index_files/OEM_Components/Flex_Cells/specification_sheets/00_FlexSolarCells.com_PowerFilm_Solar_SP3-12_Specification_Sheet.pdf. (2017).
- [7] Ujjwal Gupta, Jaehyun Park, Hitesh Joshi, and Umit Y. Ogras. 2017. Flexibility-aware system-on-polymer (SoP): Concept to prototype. *IEEE Transactions on Multi-Scale Computing Systems* 3, 1 (2017), 36–49.
- [8] InvenSense. 2017. Motion Processing Unit. https://www.invensense.com/products/motion-tracking/9-axis/mpu-9250. (2017).
- [9] Pil Gu Kang, Byung Kil Yun, Kil Dong Sung, Tae Kwon Lee, Minbaek Lee, Nuri Lee, Seol Hee Oh, William Jo, Hae Jin Seog, Chang Won Ahn, Ill Won Kim, and Jong Hoon Jung. 2014. Piezoelectric power generation of vertically aligned lead-free (K,Na)NbO₃ nanorod arrays. RSC Advances 4, 56 (2014), 29799–29805.
- [10] Sun Jin Kim, Ju Hyung We, and Byung Jin Cho. 2014. A wearable thermoelectric generator fabricated on a glass fabric. Energy & Environmental Science 7, 6 (2014), 1959–1965.
- [11] David L. King, Jay A. Kratochvil, and William Earl Boyson. 2004. *Photovoltaic Array Performance Model.* United States. Department of Energy.
- [12] Sathish Kumar Kollimalla and Mahesh Kumar Mishra. 2014. A novel adaptive P&O MPPT algorithm considering sudden changes in the irradiance. *IEEE Transactions on Energy Conversion* 29, 3 (2014), 602–610.
- [13] Christos Konstantopoulos and Eftichios Koutroulis. 2014. Global maximum power point tracking of flexible photovoltaic modules. *IEEE Transactions on Power Electronics* 29, 6 (2014), 2817–2828.
- [14] Chao Lu, Vijay Raghunathan, and Kaushik Roy. 2011. Efficient design of micro-scale energy harvesting systems. *IEEE Journal on Emerging and Selected Topics in Circuits and Systems* 1, 3 (2011), 254–266.
- [15] André Mermoud and Thibault Lejeune. 2010. Performance assessment of a simulation model for PV modules of any available technology. In *Proceedings of the 25th European Photovoltaic Solar Energy Conference*. 6–11=0.
- [16] Jens Merten, J. M. Asensi, C. Voz, A. V. Shah, R. Platz, and J. Andreu. 1998. Improved equivalent circuit and analytical model for amorphous silicon solar cells and modules. *IEEE Transactions on Electron Devices* 45, 2 (1998), 423–429.
- [17] National Instruments. 2017. PXIe-4080. http://www.ni.com/en-us/support/model.pxie-4080.html. (2017).
- [18] National Instruments. 2017. PXIe-4081. http://www.ni.com/en-us/support/model.pxie-4081.html. (2017).
- [19] Joseph A. Paradiso and Thad Starner. 2005. Energy scavenging for mobile and wireless electronics. *IEEE Pervasive Computing* 4, 1 (2005), 18–27.
- [20] Azadeh Safari and Saad Mekhilef. 2011. Simulation and hardware implementation of incremental conductance MPPT with direct control method using cuk converter. IEEE Transactions on Industrial Electronics 58, 4 (2011), 1154–1161.
- [21] Dezso Sera, Remus Teodorescu, and Pedro Rodriguez. 2007. PV panel model based on datasheet values. In IEEE International Symposium on Industrial Electronics. 2392–2396.
- [22] Pooja Sharma, Siddhartha P. Duttagupta, and Vivek Agarwal. 2012. A novel and universal model for accurate prediction of PV module characteristics for power optimization under various design layouts and dynamic environmental conditions. In *Proceedings of IEEE International Conference on Power Electronics, Drives and Energy Systems.* 1–6.

156:20 J. Park et al.

[23] Pooja Sharma, Siddhartha P. Duttagupta, and Vivek Agarwal. 2014. A novel approach for maximum power tracking from curved thin-film solar photovoltaic arrays under changing environmental conditions. IEEE Transactions on Industry Applications 50, 6 (2014), 4142–4151.

- [24] Hadeed Ahmed Sher, Ali Faisal Murtaza, Abdullah Noman, Khaled E. Addoweesh, Kamal Al-Haddad, and Marcello Chiaberge. 2015. A new sensorless hybrid MPPT algorithm based on fractional short-circuit current measurement and P&O MPPT. IEEE Transactions on Sustainable Energy 6, 4 (2015), 1426–1434.
- [25] Donghwa Shin, Naehyuck Chang, Yanzhi Wang, and Massoud Pedram. 2015. Reconfigurable three dimensional photovoltaic panel architecture for solar-powered time extension. In Proceedings of the 2015 IEEE/ACM International Symposium on Low Power Electronics and Design. 273–278.
- [26] T. Söderström, F.-J. Haug, V. Terrazzoni-Daudrix, and C. Ballif. 2008. Optimization of amorphous silicon thin film solar cells for flexible photovoltaics. *Journal of Applied Physics* 103, 11 (2008), 114509.
- [27] Spectra Symbol. 2017. Flex Sensor. http://www.spectrasymbol.com/product/flex-sensors/. (2017).
- [28] TES Electrical Electronic Corp. 2017. TES-1333. http://www.tes.com.tw/en/product_detail.asp?seq=285. (2017).
- [29] Texas Instruments. 2017. BQ25504. http://www.ti.com/lit/ds/symlink/bq25504.pdf. (2017).
- [30] Texas Instruments. 2017. CC2650. http://www.ti.com/lit/ds/symlink/cc2650.pdf. (2017).
- [31] Y.-J. Wang and P.-C. Hsu. 2010. Analytical modelling of partial shading and different orientation of photovoltaic modules. *IET Renewable Power Generation* 4, 3 (2010), 272–282.

Received February 2007; revised March 2009; accepted June 2009